Chemical Science

ROYAL SOCIETY OF CHEMISTRY

EDGE ARTICLE

View Article Online
View Journal | View Issue

Check for updates

Cite this: *Chem. Sci.*, 2025, **16**, 22046

All publication charges for this article have been paid for by the Royal Society of Chemistry

Enzyme-mimicking metal–organic framework-enabled microsensor for specific electrochemical monitoring *in vivo*

Zhao Yang,[a] Tao Huang,*[b] Fei Li,[a] Wenbo Huang,[a] Xikui Ouyang,[a] Kangbing Wu[a] and Junxing Hao *[a]

Received 2nd May 2025
Accepted 12th October 2025

DOI: 10.1039/d5sc03207e

rsc.li/chemical-science

The pursuit of specific and stable electrochemical sensing techniques is vital for probing physiological and pathological processes in the living brain. Although the widespread adoption of natural enzymes is the cornerstone of current neurochemical recognition strategies, their sensing capabilities are susceptible to failure in complex biological environments. Herein, we have synthesized an ascorbate (AA) oxidase mimic, specifically a copper metal–organic framework functionalized with histidine and tryptophan (CuMOF-HT), using a chelation-assisted selective etching method. The simulant exhibits ultrafast AA sensing properties, with a response time of 0.1 seconds, along with exceptional selectivity and reliability. This is attributed to its robust Cu catalytic centers, specific amino acid recognition sites, and water-stable MOF architectures. Furthermore, the enzyme-like CuMOF-HT is integrated onto the tip of a minimally invasive acupuncture needle, forming a microelectrode that demonstrates superior electron transfer rates, enzymatic reactivity, and monitoring stability, making it ideal for subsequent *in vivo* AA sensing. As a demonstration, the microsensor can keenly track fluctuations in AA concentrations in mouse brain models such as epileptic seizures and cytotoxic edema. More importantly, the specific recognition strategy, which mimics the function of natural enzymes, holds broad applicability for analyzing a wide range of analytes in the field of brain science.

Open Access Article. Published on 21 October 2025. Downloaded on 6/14/2026 12:59:03 PM.
This article is licensed under a Creative Commons Attribution-NonCommercial 3.0 Unported Licence.

Introduction

In brain science and brain-like research, probing neurochemical substances represents a pivotal technique for comprehending brain function and disease mechanisms.[1,2] These substances, functioning as chemical signaling molecules that convey information between neurons, directly impact cognitive and behavioral functions such as learning, memory, and emotional regulation.[3] Consequently, precise monitoring of the dynamic changes in these neurochemical substances is crucial for elucidating human cognitive brain functions, preserving brain health, and simulating brain operations. However, given the complex and transient nature of neurochemical substances within the brain, achieving rapid, sensitive, specific, and stable monitoring of neurochemical biomarkers, particularly biomolecules, poses a formidable challenge. So far, pathbreaking achievements have been reported in the development of electrochemical and biochemical sensors that utilize carbon fibers,[4,5] molecular probes,[6,7] aptamers,[8] and natural enzymes[9,10] for conducting *in vivo* analysis in the brain. Nonetheless, carbon fibers relying on potential control face challenges in achieving absolute selective detection, while molecular probes and aptamers require sufficient response time. Although natural enzymes exhibit excellent specificity and response speed, their sensing performance is unstable and highly susceptible to failure *in vivo*. Therefore, there is an urgent need to develop *in vivo* microsensors capable of achieving specific, real-time, and stable monitoring of neurochemical biomolecules.

Metal–organic framework (MOF)-based nanoenzymes,[11,12] as an innovative class of nanomaterials exhibiting enzyme-like properties, have recently attracted great attention in the fields of materials science, biochemistry, and medicine. Their distinctive structure imparts MOF-based nanoenzymes with a high specific surface area, abundant porosity, and uniform active sites, all of which contribute to their ultrafast speed and superior sensitivity during catalytic reactions.[13,14] Pioneering scientists have designed several enzyme-mimicking materials with superior electrocatalytic sites (peroxidase, oxidase, and catalase-mimics),[15,16] achieved through the precise regulation of metal nodes and organic ligands within MOFs. However, unlike natural enzymes, MOF-based nanoenzymes do not contain recognition sites for specific biomolecule binding,[17,18] leading to indiscriminate adsorption and catalysis of complex biomolecules in the brain. As a result, their casual catalytic behaviors

[a]*Ministry of Education Key Laboratory for the Synthesis and Application of Organic Functional Molecules, Hubei Province Key Laboratory of Biotechnology of Chinese Traditional Medicine, College of Health Science and Engineering, Hubei University, Wuhan 430062, China. E-mail: jxhao@hubu.edu.cn*

[b]*General Surgery, People's Hospital of Dongxihu District, Wuhan, 430040, China*

© 2025 The Author(s). Published by the Royal Society of Chemistry

Open Access Article. Published on 21 October 2025. Downloaded on 6/14/2026 12:59:03 PM.
This article is licensed under a Creative Commons Attribution-NonCommercial 3.0 Unported Licence.

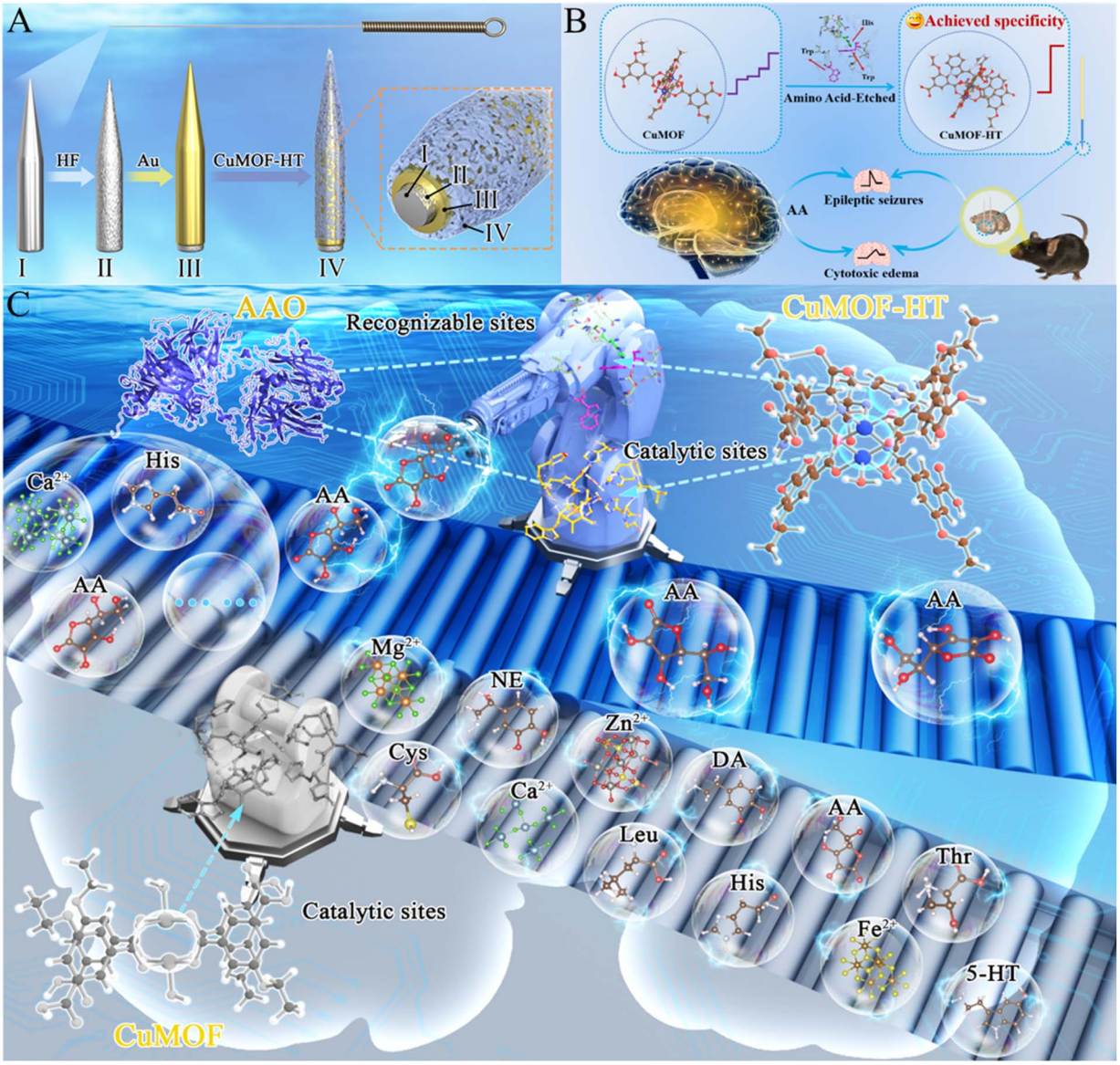

Scheme 1 Customizing CuMOF-based enzymes inspired by AAO for AA sensing *in vivo*. (A) Layer-by-layer modification of a microsensor. From inside to outside: raw stainless steel acupuncture needle (I), fluoride etching (II), electro-deposition of gold (III), and dip-coating with CuMOF-HT (IV). (B) Schematic diagram of the CuMOF-HT microsensor for highly targeted, stable, and sensitive response of AA levels in mouse brain models of epileptic seizures and cytotoxic edema. (C) The principle of specific recognition and electrochemical catalysis processes of AA by an enzyme-like CuMOF-HT.

and lack of substrate specificity make it impossible to achieve highly specific identification of neurochemical biomolecules.[19,20] Furthermore, the poor water stability of MOF-based nanoenzymes results in a gradual degradation of their electrocatalytic performance.[21,22] To enhance their stability, encapsulation with carbon layers[23,24] or polymers[25,26] is frequently employed, yet these approaches can unfortunately occlude active sites. Hence, personalizing MOF-based nanoenzymes and achieving specific recognition and stable catalysis of neurochemical biomolecules *in vivo* pose a significant challenge.

Herein, inspired by ascorbate oxidase (AAO), we introduce a copper metal–organic framework (CuMOF-HT) functionalized with two amino acids (histidine and tryptophan). This CuMOF-HT is synthesized using a chelation-assisted selective etching strategy, with the ultimate goal of achieving ultrafast, highly specific, and stable neurosensing *in vivo*. Furthermore, CuMOF-HT, which resembles the structure of AAO, can be conveniently modified onto a minimally invasive acupuncture needle *via* dip-coating (Scheme 1A), thereby creating a specific microsensor for rapid and stable recognition of ascorbate (AA). The microsensor boasts several impressive features: an ultrafast response time of 0.1 s, a remarkably low detection limit of 1.46 μM, and exceptional stability, allowing it to be stored at room temperature for over 6 months. The systematic analysis of enzymatic kinetic data, coupled with theoretical calculations, elucidates that CuMOF-HT mimics the specific catalytic mechanism of AAO. In

Open Access Article. Published on 21 October 2025. Downloaded on 6/14/2026 12:59:03 PM. This article is licensed under a Creative Commons Attribution-NonCommercial 3.0 Unported Licence.

this mechanism, amino acids play a crucial role by facilitating the specific capture and recognition of AA, which then accelerates its electrochemical oxidation at the copper sites. Finally, the CuMOF-HT-based microsensor has been successfully utilized to monitor AA levels in mouse brains exhibiting different pathological states, such as epileptic seizures and cytotoxic edema (Scheme 1B). More importantly, our findings reveal a positive correlation between the release of AA and the increased presence of agents, specifically *N*-methyl-D-aspartic acid (NMDA), that induce cytotoxic edema. In addition, inhibiting cytotoxic edema with 4,4′-diisothiocyanatostilbene-2,2′-disulfonic acid (DIDS) leads to the cessation of AA release, further supporting the notion that AA efflux is dependent on the occurrence of cytotoxic edema. This work not only uncovers the ultrafast catalytic properties of MOF-based nanoenzymes but also lays the foundation for achieving specific and stable *in vivo* neurosensing.

Results and discussion

Characterization of enzyme-like CuMOF materials

AA is a key neurochemical biomolecule that plays indispensable roles in a wide array of physiological and pathological processes within the brain.[27] It exhibits several beneficial properties, including combating scurvy, providing neuroprotection in cases of brain injuries, modulating neurological functions, and facilitating stem cell differentiation.[28] Therefore, the achievement of ultrafast, specific, and stable *in vivo* sensing of AA is crucial for accurately assessing and mitigating the risks associated with these diseases. As illustrated in Scheme 1C, AAO possesses the capability to specifically recognize and oxidize AA, leveraging a pocket structured with histidine (His) and tryptophan (Trp) residues, along with copper sites.[29] Essentially, the specific binding affinity of AAO arises from the strong interaction between His/Trp and AA, while its oxidation relies on copper's redox properties. Based on this, CuMOF,[30] which exhibits remarkable hydrolytic stability, has been chosen to mimic natural AAO. This choice is attributed to CuMOF's kagome-like topology, centered around Cu paddle-wheel clusters, which potentially displays electro-oxidative behavior towards AA under an electrical field. However, pristine CuMOF lacks a selective recognition site for AA. Hence, we tried to induce capture behavior of CuMOF towards AA by incorporating His/Trp into the Cu paddle-wheel cluster through a chelation-assisted selective etching strategy (Fig. S1), aiming to create its specificity.

At first, $Cu(CH_3COO)_2 \cdot H_2O$ is chosen to induce the formation of CuMOF due to its similar crystal axes (Fig. S2). As depicted in Fig. 1A, the X-ray diffraction (XRD) patterns confirm that CuMOF can be successfully prepared using $Cu(CH_3COO)_2 \cdot H_2O$ as the copper precursor. It is noteworthy that CuMOF-HT displays no new XRD peaks, suggesting that the crystal structures of CuMOF largely remain intact after His/Trp etching at suitable concentrations, without any ligand exchange reaction taking place. Besides, digital camera images revealed a fine and smooth powder of CuMOF, in contrast to the random and shaggy appearance of CuMOF-HT (Fig. S3). Field emission scanning electron microscopy (FESEM) and transmission electron microscopy (TEM) images show the hexagonal prism structure of CuMOF, characterized by its smooth surface and well-defined layered stacking, as illustrated in Fig. 1B, S4A and C. Although some irregular small pores are distinctly visible on the surface of CuMOF-HT, the hexagonal prism structure remains (Fig. 1C, S4B and D). The pore size relies on the concentration of His and Trp, and a higher concentration will result in serious damage to the CuMOF structure (Fig. S5). Furthermore, high-resolution transmission electron microscopy (HRTEM) reveals smooth and even internal exfoliation layer within CuMOF-HT (Fig. S4E). The electron diffraction pattern from a selected area of these inner stripped layers (Fig. S4F) indicates an ordered (270) lattice, confirming its single-crystal structure.[31] Noteworthily, the defects present in the crystals arise due to the etching effect of Lewis acids, as evidenced by the HRTEM image, which further shows that the etching of His and Trp is confined to the crystal surface. The intact crystal structure of CuMOF-HT suggests that amino acid absorption primarily occurs on the CuMOF surface, with minimal penetration of His or Trp into the micropores. Elemental mapping analysis validates the successful incorporation of amino acids onto the surface of CuMOF-HT crystals (Fig. 1D and S6).

Attenuated total reflectance infrared (ATR-IR) spectroscopy was also utilized to analyze both CuMOF and CuMOF-HT. Fig. 1E illustrates that the peaks located at 3390 and 3340 cm^{-1} signify N–H scissoring vibrations, while the peak at 3269 cm^{-1} represents NH stretching vibrations. Other notable peaks include those at 2910, 1220, 854, and 580 cm^{-1}, which are associated with O–H stretching in COOH, C–NH– stretching, in-plane rocking of N–H, and out-of-plane deformation of O–H in Trp, respectively. Additionally, the peaks at 1130 and 820 cm^{-1} correspond to C=N–C stretching and in-plane rocking vibrations of N–H in His, respectively. Notably, CuMOF-HT exhibits a distinct peak at 694 cm^{-1}, attributed to N–Cu– stretching vibrations, indicative of Cu–N bonding. Furthermore, there is an increase in Cu–O stretching from 494 to 496 cm^{-1}, which is attributed to the coordination of NH_2 to the Cu paddle wheel structure. These ATR-IR findings suggest that His and Trp bind to the Cu paddle wheel on CuMOF-HT, confirming this structure as the binding site for these amino acids.[32] In addition, the calculation of the His/Trp ratio yields a value of 2.01 through normalization based on a shared peak (O–H out-of-plane bending) found in both His and Trp (Fig. S7). Consequently, the initial amino acid ratio utilized for treatment was set at 2 : 1. Based on above ATR-IR findings, –HN–Cu forms through two mechanisms. Firstly, it arises from direct axial coordination with amino acids. Secondly, amino acids connect to ligands *via* surface disruptions on the Cu paddle wheel, facilitated by the activation of carbonyl carbon due to the Lewis acid property of Cu.[33] Thus, six potential spatial structures of His and Trp on the Cu paddle wheel are identified, as depicted in Fig. S8. Given the His/Trp ratio of 2 : 1 on the CuMOF-HT surface, the most plausible structure involves one His axially coordinated to Cu, with two Trp ligands bound to Cu on either side. This arrangement allows for the central amino acid to be shared,

 © 2025 The Author(s). Published by the Royal Society of Chemistry

Open Access Article. Published on 21 October 2025. Downloaded on 6/14/2026 12:59:03 PM. This article is licensed under a Creative Commons Attribution-NonCommercial 3.0 Unported Licence.

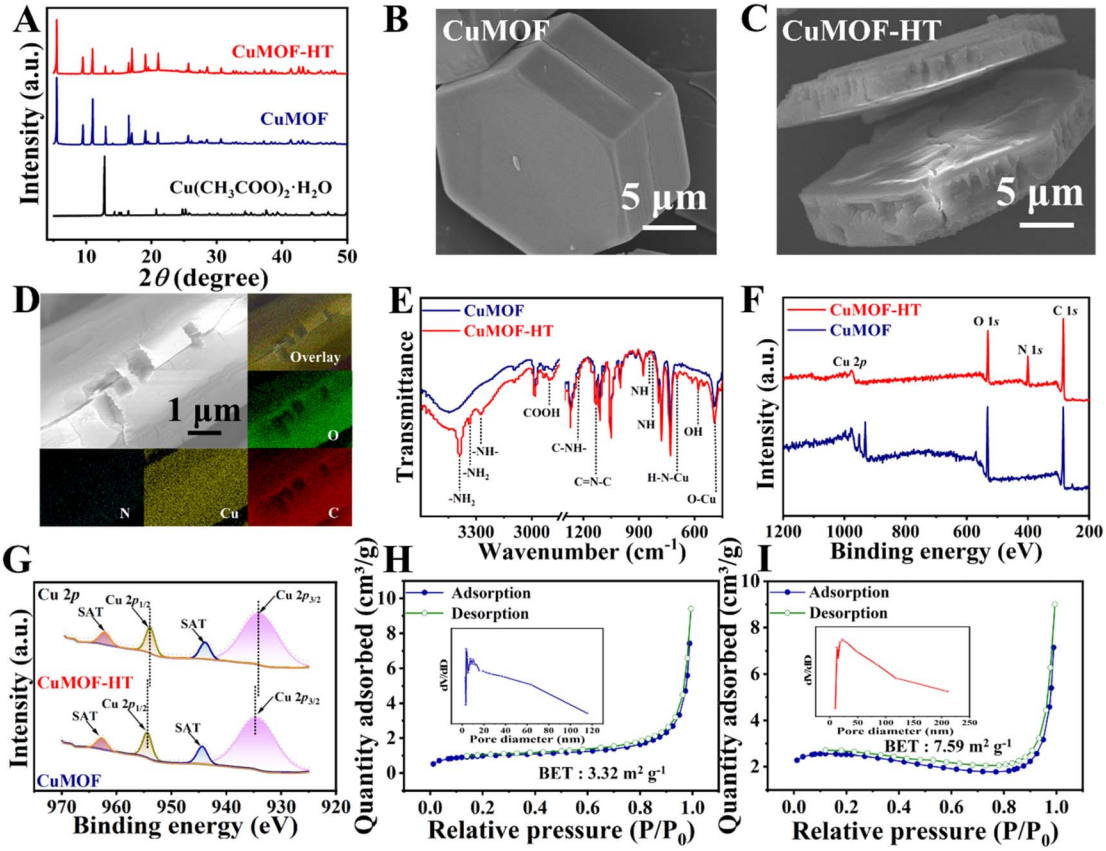

Fig. 1 (A) XRD patterns of $Cu(CH_3COO)_2 \cdot H_2O$, CuMOF and CuMOF-HT. FESEM images of (B) CuMOF and (C) CuMOF-HT. (D) FESEM images of cubic defects on CuMOF-HT and corresponding overlap elemental mapping. Corresponding elemental C, O, N, and Cu mapping images of CuMOF-HT. (E) ATR-IR spectra of CuMOF and CuMOF-HT. (F) XPS results for CuMOF and CuMOF-HT. (G) Cu 2p for CuMOF and CuMOF-HT. N_2 adsorption–desorption isotherms and pore-size distributions of (H) CuMOF and (I) CuMOF-HT.

enhancing the combined effect of His and Trp. These His/Trp configurations on the Cu paddle wheel are predominant on the CuMOF surface and are crucial for AA selectivity.

X-ray photoelectron spectroscopy (XPS) was performed to analyze the elemental compositions and valence states of both CuMOF and CuMOF-HT materials (Fig. 1F, G and S9). The total survey spectrum clearly shows peaks corresponding to Cu 2p, C 1s, O 1s, and N 1s. Notably, the distinct N peak (~5.5%, Table S1) confirms successful amino acid functionalization on the CuMOF surface. Additionally, the valence state distribution reveals a 0.5 eV binding energy shift for Cu 2p in CuMOF-HT, and electron paramagnetic resonance (EPR) further detects an additional Cu^{2+} resonance signal in CuMOF-HT (Fig. S10). These findings suggest a different surface Cu coordination structure in CuMOF-HT compared to CuMOF, confirming the coordination interactions between His and Trp with Cu.

The N_2 adsorption–desorption isotherms were employed to assess the specific surface areas and pore size distributions of CuMOF and CuMOF-HT (Fig. 1H and I). Brunauer–Emmett–Teller (BET) analysis revealed that CuMOF-HT exhibited a significantly higher specific surface area (7.59 $m^2\ g^{-1}$) compared to CuMOF (3.32 $m^2\ g^{-1}$). This enhancement in BET value for CuMOF-HT can be attributed to the His and Trp chelation-assisted selective etching effect. The pore size distribution curves (insets in Fig. 1H and I) indicate that CuMOF and CuMOF-HT exhibit pores primarily centered at 3.78 nm and 22.97 nm, respectively, implying an abundant mesoporous structure. In addition, their average pore sizes, calculated as 25.89 nm for CuMOF and 46.64 nm for CuMOF-HT, confirm that amino acid treatment enhances larger pores within the MOF structure. In a word, CuMOF-HT possesses a large surface area and abundant porosity, enhancing active site exposure and promoting interfacial mass diffusion and electron transfer.

Michaelis–Menten kinetics of enzyme-like CuMOF materials

Given the striking similarity in the local structure between CuMOF-HT and natural AAO,[34] both of which possess a Cu catalytic center along with two amino acid recognition sites, we hypothesize that CuMOF-HT demonstrates potential AAO-mimetic characteristics. Thereafter, we evaluated the catalytic activity of CuMOF-HT as an AAO mimic, employing AA as the substrate, at a simulated human body temperature of 37 °C (Fig. 2A), and contrasted its performance against the control group. As shown in Fig. 2B, the absorbance at $\lambda_{max} = 265$ nm was measured for various AA concentrations using a standard solution. A standard curve was plotted (Fig. 2C), revealing

Open Access Article. Published on 21 October 2025. Downloaded on 6/14/2026 12:59:03 PM.
This article is licensed under a Creative Commons Attribution-NonCommercial 3.0 Unported Licence.

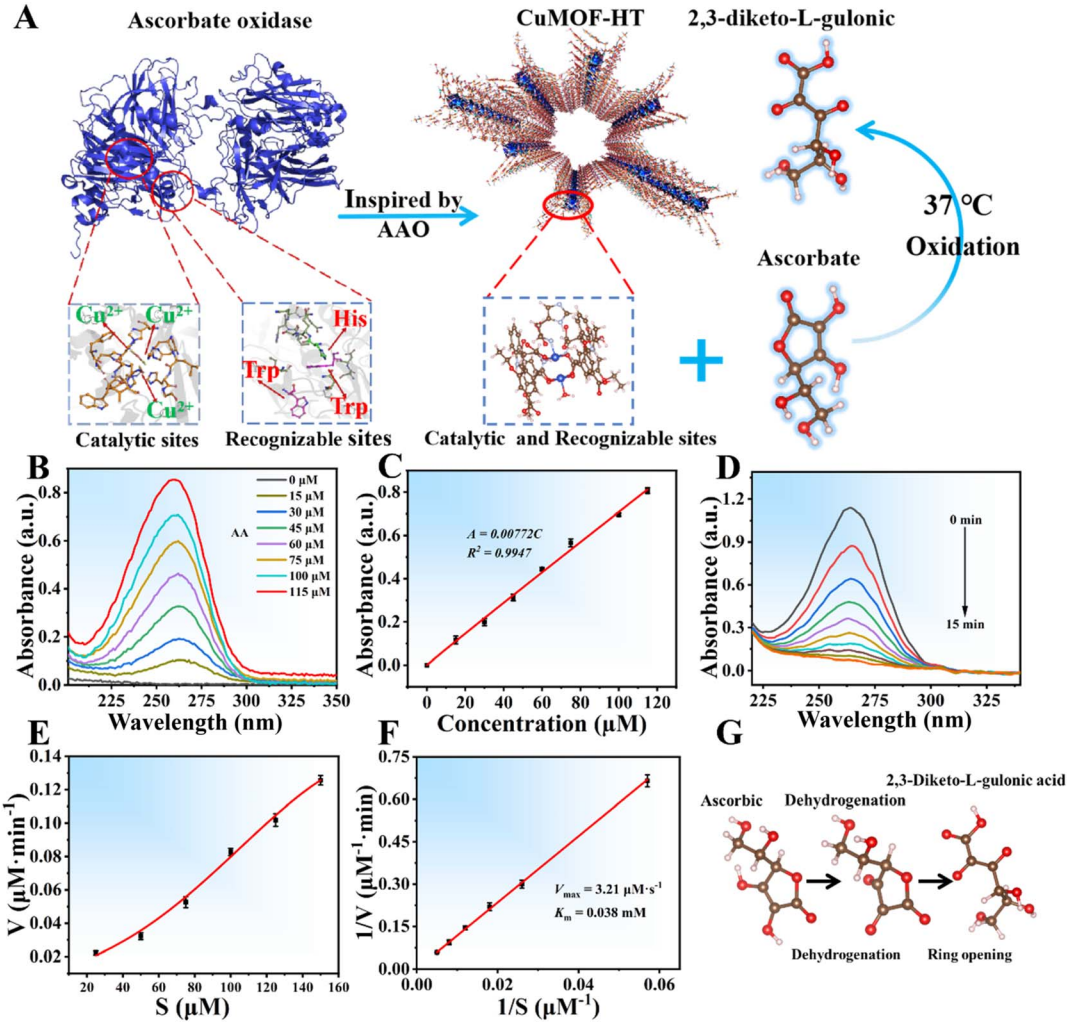

Fig. 2 (A) Reaction showing oxidation of AA by CuMOF-HT. (B) UV absorption curves of AA oxidation. (C) The plot of absorbance *versus* AA concentration. (D) Absorbance spectra of AA in the presence of CuMOF-HT over time. (E) CuMOF-HT sample AA oxidase activity of steady-state kinetics. (F) Lineweaver–Burk curve of AA oxidase-like activity of CuMOF-HT. Error bar represents the relative standard deviation of three measurements ($n = 3$). (G) The AA electrooxidation pathway is depicted using a ball-and-stick model, in which the blue, red, brown, and gray spheres correspond to Cu, O, C, and H atoms, respectively.

a direct proportionality between AA concentration and absorbance. Subsequently, both the CuMOF-HT and control samples were fully suspended in a 0.1 M PBS buffer (pH = 7.4), and the AA substrate was added to the mixture to achieve a final concentration of 100 μM. We monitored the consumption of AA using a UV spectrometer ($\lambda_{max} = 265$ nm) to measure the catalytic process and assess various sample performances. As illustrated in Fig. 2D, as the catalytic reaction of CuMOF-HT progressed, the concentration of AA decreased, resulting in a corresponding decrease in absorbance.

To identify the optimal design for enzyme-mimicking CuMOF-HT, a series of samples were synthesized *via* an amino acid-selective etching method, with variations in His/Trp ratios, concentrations, and etching durations. Afterwards, their catalytic performances were compared under identical reaction conditions (Fig. S11). The results indicated that the CuMOF-HT prepared with a His/Trp ratio of 1 : 2, His concentration of 5 mM, Trp concentration of 10 mM, and etched for 12 h, exhibited the most favorable catalytic performance. In addition, to confirm that the selective oxidation of AA stems from CuMOF-HT, we designed both experimental and control groups, using the chemical formula of CuMOF-HT as a basis and incorporating specific masses as detailed below: blank (0 mg), His (0.39 mg), Trp (0.15 mg), 5-ethoxyisophthalic acid (1.29 mg), $Cu(CH_3COO)_2 \cdot H_2O$ (0.60 mg), CuMOF (1.50 mg), and CuMOF-HT (1.50 mg). As depicted in Fig. S12, the enzyme-mimicking CuMOF-HT exhibited the highest level of catalytic activity for the oxidation of AA. As expected, the CuMOF suspension demonstrated restricted catalytic activity, indicating an initial oxidation rate towards AA that was approximately half of that observed for CuMOF-HT. On the other hand, the blank or solutions containing only the Cu^{2+}, ligand, or amino acid, show a further weakened capability of oxidizing AA. Therefore, the CuMOF-HT structure played a crucial role in its

© 2025 The Author(s). Published by the Royal Society of Chemistry

Open Access Article. Published on 21 October 2025. Downloaded on 6/14/2026 12:59:03 PM. This article is licensed under a Creative Commons Attribution-NonCommercial 3.0 Unported Licence.

catalytic behavior. Specifically, coordination of one His and two Trp on the copper paddlewheel formed pocket-like structures. These pockets, with their appropriate geometry, effectively bound ascorbate through π–π stacking and hydrogen bonds,[35] creating a staggered system involving ascorbate's lactone ring and the side chains of Trp and His. For AAO, the skeleton comprising copper and His/Trp served as both the active catalytic center and recognition site. A very similar structure reoccurred, functioning in the oxidation of AA, both at the surface and interior of CuMOF-HT.

The steady-state behavior of these catalytic reactions can be analyzed using the Michaelis–Menten kinetics (Fig. 2E and S13A) and Lineweaver–Burk plot (Fig. 2F and S13B). Both plots are derived from experimental data, where the concentration of AA was varied from 25 to 150 μM, while the amounts of CuMOF or CuMOF-HT remained constant at 1.5 mg. The linear regression analysis conducted on the Lineweaver–Burk plots reveals that the oxidation of AA facilitated by CuMOF and CuMOF-HT adheres to kinetics that mimic those of enzymes. The maximal initial rates (V_{max}) for CuMOF and CuMOF-HT, derived from their respective plots, were 3.21 μM s^{-1} and 0.052 μM s^{-1}, with corresponding Michaelis constants (K_m) of 0.038 mM and 0.56 mM, respectively. Comparative analysis with natural AAO and other documented nanoenzymes (Table S2) reveals that enzyme-mimicking CuMOF-HT demonstrates a significantly higher V_{max} value, while retaining a K_m value comparable to that of AAO. Besides, high-resolution mass spectrometry (HRMS) characterization identified 2,3-diketo-L-gulonic acid as the primary oxidative derivative of AA following treatment with CuMOF-HT (Fig. S14). The AA oxidation mechanism, as illustrated in Fig. 2G, initiates with the binding of AA to Trp/His residues on the Cu paddle wheel structure. The highly oxidative Cu center facilitates rapid dehydrogenation of the bound substrate, resulting in the formation of dehydroascorbic acid. Subsequent oxidative ring cleavage converts this intermediate into 2,3-diketo-L-gulonic acid. Following the completion of the oxidation cycle, the product dissociates from the Trp/His coordination sites, thereby regenerating the catalytic center for subsequent substrate molecules.

Electrochemical properties of enzyme-like CuMOF materials

Following a comprehensive characterization of the physical properties and enzyme-like activity of the CuMOF-HT material, which demonstrates AA oxidase-like behavior, we employed CuMOF-HT as the AA recognition and sensing element to develop a highly sensitive, selective, and stable microelectrode. The successful preparation of NEG-CuMOF-HT was confirmed through meticulous characterization of each stage of the process using FESEM, as illustrated in Fig. S15. First, the electrochemical characteristics of as-proposed N, NE, NEG, NEG-CuMOF, and NEG-CuMOF-HT electrode materials were evaluated using cyclic voltammetry (CV) with a redox probe ($K_3/K_4[Fe(CN)_6]$). As shown in Fig. 3A, the peak currents of NEG and NEG-CuMOF exhibit a significant increase compared to those of N and NE, demonstrating that the incorporation of gold and CuMOF effectively enhances the number of electrochemical active sites and accelerates electron-transfer rates. Furthermore, the NEG-CuMOF-HT composites reveal the smallest anodic–cathodic peak potential separation (ΔE_p) and the highest oxidation peak current values (I_{pa}), reflecting their exceptional electron-transfer capability. Subsequently, electrochemical impedance spectroscopy (EIS) of $K_3/K_4[Fe(CN)_6]$ on various electrode materials was performed to investigate electrode kinetics. As illustrated in Fig. 3B, the semicircle diameter corresponds to the charge transfer resistance (R_{ct}), with smaller R_{ct} values indicating faster electron transfer rates.[36,37] Using the Randles equivalent circuits shown in the inset of Fig. 3B, the fitted R_{ct} values for N, NE, NEG, NEG-CuMOF, and NEG-CuMOF-HT are 16490.08, 13953.24, 2.62, 1.89, and 0.92 KΩ, respectively. Notably, the NEG-CuMOF-HT composites exhibit significantly enhanced charge-transfer capabilities, consistent with the CV results presented in Fig. 3A.

The electrochemical performance of NEG-CuMOF-HT was further evaluated using chronoamperometry (*i*–*t*) with successive additions of AA in 0.1 M PBS. As indicated in Fig. 3C, the steady-state current response of NEG-CuMOF-HT to AA is approximately 2040 and 3 times greater than that of NEG and NEG-CuMOF, respectively, demonstrating its superior electrochemical activity for AA sensing, which is attributed to the copper catalytic centers and amino acid recognition sites. Meanwhile, we validated our hypothesis that CuMOF-HT exhibits the most significant change in current response (ΔI) only when His and Trp simultaneously chelate the CuMOF (Fig. S16). Additionally, we investigated the effects of CuMOF-HT loading concentration, electrodeposition duration of gold nanoparticles, and applied potential (Fig. S17). Based on a comprehensive consideration of efficiency and energy consumption, the optimal working conditions are as follows: a CuMOF-HT concentration of 2 mg mL^{-1}, a gold electrodeposition duration of 90 s, and a working potential of – 0.2 V.

To further validate the superior electrochemical reactivity of the NEG-CuMOF-HT composites, the electrochemical surface area (ECSA) of each electrode material was evaluated. Fig. S18 shows a series of CV tests performed in KCl within the non-faradaic potential range (0.15–0.25 V) at varying scan rates (25–200 mV s^{-1}). As shown in Fig. 3D, the current density at 0.20 V ($\Delta j_{0.20\ V}$) increases significantly with higher scan rates. From the slope (k), the double-layer capacitance ($C_{dl} = k/2$) was calculated to be 0.00041, 0.0012, 0.0054, 0.007, and 0.0094 μF cm^{-2} for N, NE, NEG, NEG-CuMOF, and NEG-CuMOF-HT, respectively. Given that the ECSA is directly proportional to C_{dl},[38] these results confirm that the NEG-CuMOF-HT composites possess a greater number of active sites and improved electrochemical reactivity. To assess the electrical conductance (G) of the electrode materials,[39] *I*–*V* curves were recorded for CuMOF and CuMOF-HT. A scanning potential ranging from −1.0 to + 1.0 V was applied in 0.1 M PBS at 0.10 V increments (Fig. 3E). Analysis of the *I*–*V* curves revealed the G values for the two materials. Notably, CuMOF-HT demonstrated significantly enhanced electron conduction capacity (14.3×10^{-9} S cm^{-1}) compared to CuMOF (9.2×10^{-9} S cm^{-1}), consistent with the CV, EIS, *i*–*t*, and ECSA results presented earlier (Fig. S19).

Open Access Article. Published on 21 October 2025. Downloaded on 6/14/2026 12:59:03 PM.
This article is licensed under a Creative Commons Attribution-NonCommercial 3.0 Unported Licence.

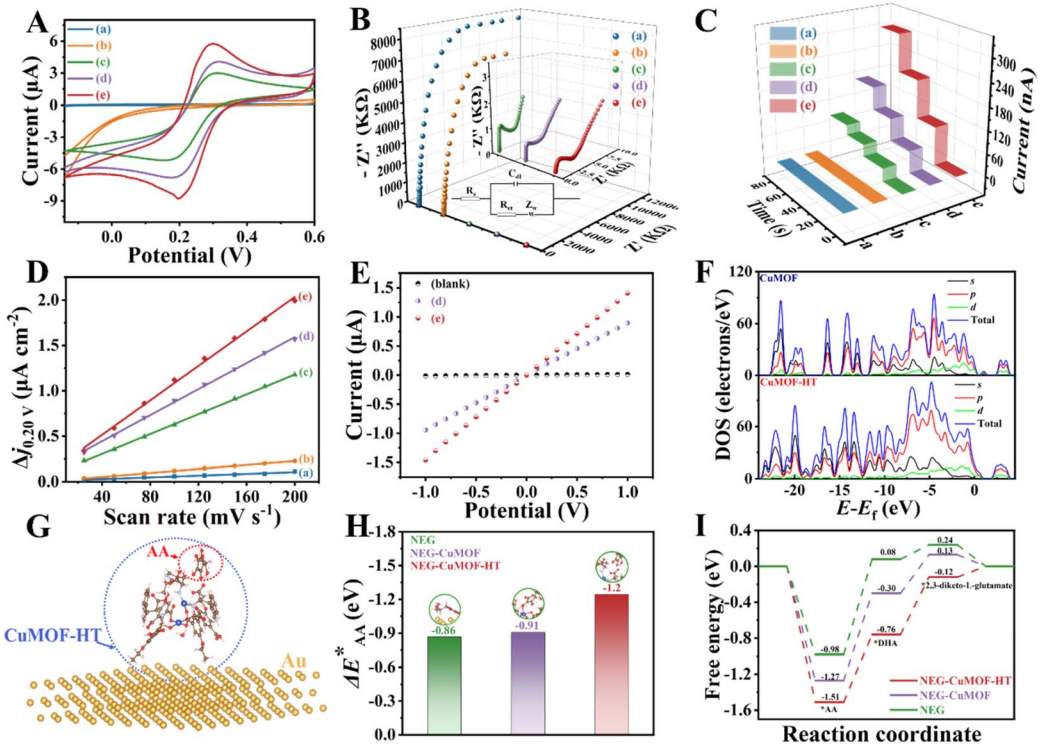

Fig. 3 (A) CVs of 5 mM $K_3/K_4[Fe(CN)_6]$ in 0.1 M KCl on N (a), NE (b), NEG (c), NEG-CuMOF (d), and NEG-CuMOF-HT (e). Scan rate: 50 mV s^{-1}. (B) Nyquist plots of 5 mM $K_3/K_4[Fe(CN)_6]$ in 0.1 M KCl on these electrodes (frequency, 0.1 Hz to 100 kHz; amplitude, 5 mV). (C) Chronoamperometry (i–t) curves of these electrodes at 0 V for 200 μM AA in 0.1 M PBS (pH = 7.4). (D) Capacitive current as a function of the scan rate for these electrodes at 0.20 V. (E) I–V curves of 0.1 M PBS (pH = 7.4) on these electrodes. Step voltage: 0.10 V. (F) DOS for CuMOF and CuMOF-HT. (G) Optimized structural models illustrating the adsorption sites for AA on NEG-CuMOF-HT. (H) Corresponding binding energy of AA on NEG, NEG-CuMOF, and NEG-CuMOF-HT. (I) Gibbs free energy diagrams of the AA oxidation on NEG, NEG-CuMOF, and NEG-CuMOF-HT.

To gain a deeper understanding of the exceptional electrocatalytic activity exhibited by CuMOF-HT towards AA oxidation, density functional theory (DFT) calculations were conducted. Initially, the Mulliken populations of both CuMOF and CuMOF-HT were computed to analyze their electronic structures. As illustrated in Fig. S20, the two Cu atoms in CuMOF-HT possess lower Mulliken charges compared to those in CuMOF, which aligns well with the previous Cu 2p XPS results (Fig. 1G). This observation suggests the presence of strong electronic interactions between His and Trp residues with CuMOF. Furthermore, Fig. 3F depicts the density of states (DOS) for both CuMOF and CuMOF-HT. Notably, due to orbital coupling among the N, C, O, H, and Cu atoms, the peaks near the Fermi energy in CuMOF-HT are more pronounced compared to those in CuMOF. This indicates that CuMOF-HT possesses a higher reactivity than CuMOF, potentially facilitating the kinetics of AA oxidation.

In the realm of heterogeneous catalysis, the adsorption of reactants holds paramount importance. Therefore, we further conducted an in-depth investigation into the binding energies of AA on NEG, NEG-CuMOF, and NEG-CuMOF-HT. The respective models, both before and after AA adsorption, are depicted in Fig. S21 and 3G. Herein, the identified active sites include the CuMOF surface and the amino acid pocket. In addition, the calculated binding energies of AA with these sensing interfaces are – 0.86, – 0.91, and – 1.2 eV, respectively (Fig. 3H). A significant enhancement in the binding energy of AA is observed on the CuMOF-HT surface, which facilitates the interaction between the amino acid active site and AA, thereby substantially improving the electrochemical sensing performance for AA.

Subsequently, we also studied the entire reaction pathways for catalyzing AA oxidation by NEG, NEG-CuMOF, and NEG-CuMOF-HT (Fig. 3I). In the case of NEG-CuMOF-HT, the formation steps of dehydroascorbate and 2,3-diketo-L-glutamate, as well as the desorption step of 2,3-diketo-L-glutamate,[40] are endothermic, with energy barriers of 0.75, 0.64, and 0.12 eV, respectively. Obviously, the rate-determining step (RDS) for NEG-CuMOF-HT is the formation of dehydroascorbate. Both NEG and NEG-CuMOF exhibit the same RDS, with energy barriers of 1.06 and 0.97 eV, respectively. The notably lower RDS energy barrier (0.75 eV) of NEG-CuMOF-HT contributes to its exceptional electrocatalytic activity for AA. Thus, the combined experimental findings and theoretical calculations suggest that NEG-CuMOF-HT operates through a mechanism analogous to natural enzymes. Specifically, the amino acid facilitates the specific capture and recognition of AA, followed by its rapid oxidation on the Cu catalytic site.

Analytical performance of the NEG-CuMOF-HT-Zw-based electrochemical microsensor for *in vitro* detection of AA

Zwitterionic polymers,[41] characterized by their high biocompatibility, ultra-low immunogenicity, antigenicity, and exceptional hydrophilicity, have attracted substantial attention in the

© 2025 The Author(s). Published by the Royal Society of Chemistry

Open Access Article. Published on 21 October 2025. Downloaded on 6/14/2026 12:59:03 PM. This article is licensed under a Creative Commons Attribution-NonCommercial 3.0 Unported Licence.

area of antifouling for *in vivo* detection. These polymers demonstrate a remarkable capacity to emulate cell membranes, which consist of proteins and phospholipids, thereby effectively reducing nonspecific protein adsorption and cell attachment. Herein, a zwitterionic sulfobetaine-3,4-ethylenedioxythiophene (SBEDOT) monomer was *in situ* electropolymerized onto an NEG-CuMOF-HT electrode to form a densely packed film, designated as NEG-CuMOF-HT-Zw. The electrocatalytic efficacy of the NEG-CuMOF-HT-Zw interface towards 200 μM AA was evaluated using *i*–*t* curves in 0.1 M PBS. Compared to the pristine NEG-CuMOF-HT composites, the electrodeposition of Zw onto the NEG-CuMOF-HT surfaces resulted in a slight decrease (<4.6%) in the current response during AA electrochemical sensing (Fig. S22). This decrease can be ascribed to the heightened interface transfer resistance induced by the electrode-coupled semiconductor polymer film. Nevertheless, the interface retained a commendable sensing signal for AA. Additionally, we investigated the analytical capabilities of the Zw-decorated NEG-CuMOF-HT microelectrode for the *in vitro* quantification of AA. As shown in Fig. 4A, S23A and D, the three types of microelectrodes (NEG-CuMOF-HT-Zw, NEG-AAO-Zw, and NEG-CuMOF-Zw) demonstrate admirable reproducibility, with respective RSDs of their current response signals being 1.7%, 3.3%, and 2.7%. The electrode modification strategies, specifically dip-coating and electropolymerization, did not significantly affect reproducibility across different electrode batches. Henceforth, the sensitivity of the NEG-CuMOF-HT-Zw towards AA was further evaluated through a series of amperometric response signals (Fig. 4B). These results revealed a linear relationship with corresponding AA concentrations ranging from 5 μM to 1.0 mM, exhibiting a sensitivity of 4.18 nA mm^{-2} μM^{-1}, and a detection limit of 1.46 μM (S/N = 3). When compared with the recently reported electrochemical AA sensors, the NEG-CuMOF-HT-Zw microsensor exhibits notably superior sensing performance, as evidenced in Table S3. In addition, the sensitivities of NEG-AAO-Zw and NEG-CuMOF-Zw for AA were also assessed (Fig. S23B, C, E and F). However, their sensing performances, encompassing linear range, sensitivity, and detection limit, were all inferior to those of NEG-CuMOF-HT-Zw.

The 1-hour amperometric stability test (Fig. 4C) revealed stark contrasts in performance: NEG-CuMOF-HT-Zw exhibited minimal current decay (3.96%), while NEG-CuMOF-Zw and NEG-AAO-Zw suffered significant losses of 22.87% and 92.37%, respectively. The catastrophic failure of NEG-AAO-Zw (>90% signal loss) directly correlates with the rapid deactivation of natural AAO enzymes under operational stress, underscoring their intrinsic instability. To further validate stability, the NEG-CuMOF-HT-Zw microelectrode was subjected to continuous 200 μM AA additions in PBS over 1 hour (Fig. S24), demonstrating negligible signal variation (RSD < 1.2%), consistent with its low decay rate (3.96%). Long-term hydrolytic stability was also confirmed through XRD and electrochemical analyses after six months of water immersion. As shown in Fig. S25A, CuMOF-HT retained its crystallinity and structural integrity, with no

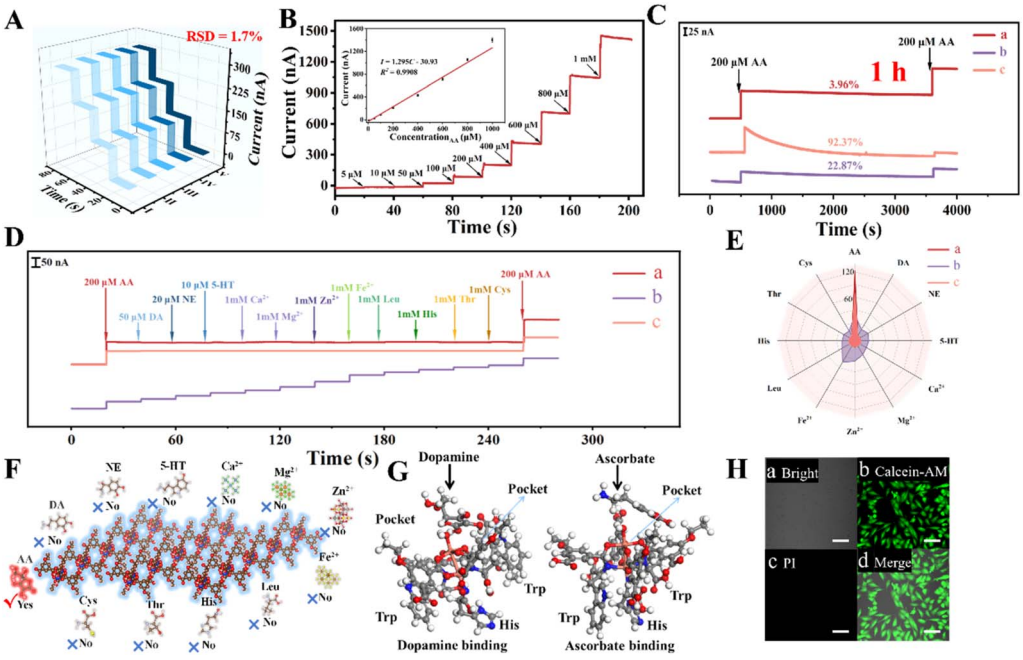

Fig. 4 (A) Reproducibility of five different NEG-CuMOF-HT-Zw microelectrodes for 200 μM AA. (B) Amperometric responses of various AA concentrations (5 μM to 1 mM). Inset: calibration curve for AA on NEG-CuMOF-HT-Zw. The error bars indicate RSD derived from triplicate measurements. (C) Comparison of amperometric response stability for AA among NEG-CuMOF-HT-Zw (a), NEG-AAO-Zw (b), and NEG-CuMOF-Zw (c), evaluated through a 1-hour *in vitro* test. (D) Selectivity evaluation of these microelectrodes (a–c) upon successive addition of AA and interfering substances. (E) Radar chart of normalized current responses of these microelectrodes (a–c) for AA and interfering substances. (F) Illustration of specific capture of AA by His/Trp residues on CuMOF-HT. (G) Optimized geometric structure for dopamine and ascorbate adsorption. (H) Confocal fluorescence imaging of HUVEC cultured on CuMOF-HT for 48 h, costained with calcein-AM (for live cells) and propidium iodide (for dead cells). Scale bar: 50 μm.

Open Access Article. Published on 21 October 2025. Downloaded on 6/14/2026 12:59:03 PM. This article is licensed under a Creative Commons Attribution-NonCommercial 3.0 Unported Licence.

detectable phase degradation. Concurrently, aged samples exhibited stable *i*–*t* responses (RSD < 2.3%, Fig. S25B), indicating its robustness under prolonged aqueous exposure.

The specificity of NEG-CuMOF-HT-Zw microsensors is critical for the accurate monitoring of AA in the brain, given the abundance of electroactive interferents such as neurotransmitters (DA, NE, and 5-HT), ions (Ca^{2+}, Mg^{2+}, Zn^{2+}, and Fe^{2+}), and amino acids (Leu, His, Thr, and Cys). As shown in Fig. 4D, NEG-CuMOF-HT-Zw exhibited a pronounced current increase upon exposure to 200 μM AA, while showing negligible responses to other interfering substances, confirming its exceptional selectivity for AA. Control experiments with NEG-CuMOF-Zw (lacking recognition sites) and NEG-AAO-Zw (natural AAO-based) revealed key limitations: the former displayed poor selectivity due to the absence of recognition sites, while the latter, despite good selectivity and moderate sensitivity, suffered rapid inactivation (>90% signal loss in stability tests), severely compromising reliability. The radar chart (Fig. 4E) further highlights the AA-specificity of NEG-CuMOF-HT-Zw, which stems from its engineered His and Trp pocket structure (Fig. 4F and S26). This architecture enables synergistic AA recognition through hydrogen bonding and π–π stacking interactions, while steric exclusion of non-target biomolecules ensures robust and selective detection in complex physiological environments.

To elucidate the specific roles of Trp/His in the enzyme-mimetic behavior of CuMOF-HT, we performed DFT calculations to investigate their interactions with AA and DA, the latter being a major endogenous interferent in cerebral monitoring, as indicated in Fig. 4G. After geometric optimization, the structure revealed that one His and two Trp residues coordinate with the copper paddle-wheel unit, forming two distinct pocket-like configurations. In the case of AA binding, the lactone ring and multiple hydroxyl groups of AA are effectively immobilized within the Trp/His pocket through a combination of π–π stacking and hydrogen bonding, leading to a staggered arrangement involving the AA lactone ring and the side chains of Trp and His. In contrast, DA interacts with the same binding pocket through only one hydrogen bond. The calculated adsorption energy for AA was −1.995 eV, more negative than that for DA, indicating a thermodynamically more favorable binding of AA. This result reasonably explains the experimentally observed selectivity of the sensor toward AA.

Given the direct contact of NEG-CuMOF-HT-Zw with living brain tissue, we evaluated its biocompatibility through cytotoxicity studies[42] using human umbilical vein endothelial cells (HUVECs). Confocal fluorescence imaging (Fig. 4H and S27) revealed a HUVEC survival rate more than 99% after 48-hour exposure, confirming exceptional biosafety. These results, combined with the enzyme-like material's high sensitivity, selectivity, repeatability, and operational stability, demonstrate its suitability for *in vivo* electrochemical monitoring of AA in the brain. The biocompatibility of the intracortically implanted sensors was evaluated by H&E staining of the brain tissue surrounding the implantation site (Fig. S28). Histopathological analysis revealed no significant inflammatory cell infiltration, tissue damage, or fibrosis at any observed time point (days 14 and 28), with tissue conditions comparable to the baseline (day 0) control. Furthermore, all biochemical and routine blood parameters across all mouse groups remained within normal ranges (Fig. S29). These collective findings confirm the favourable biocompatibility and support the safety of our sensors for long-term intracerebral implantation.

Feasibility of the NEG-CuMOF-HT-Zw-based sensing system for *in vivo* analysis

Ascorbate, also known as vitamin C, stands out as one of the most prevalent antioxidants in the mammalian central nervous system (CNS).[43] It plays a pivotal role in neuromodulation, neuroprotection, and maintaining redox homeostasis. In addition to its crucial involvement in the synthesis and metabolism of neurotransmitters, AA actively scavenges free radicals, thereby safeguarding neurons from oxidative stress-induced damage. Recent evidence has shown that abnormal levels of AA are closely associated with a variety of neurological disorders, including epilepsy, cerebral edema, Parkinson's disease, and cerebral ischemia-reperfusion injury.[44] Therefore, it is imperative to conduct real-time, rapid, and specific monitoring of dynamic fluctuations of AA in the brain, in order to elucidate its physiological functions and decipher the pathological mechanisms underlying these CNS-related conditions. Building upon this foundation, we have designed a highly sensitive, selective, and stable electrochemical microsensor (NEG-CuMOF-HT-Zw), which serves as a reliable platform for monitoring cerebral AA levels. This microsensor enables real-time tracking of AA dynamics within the complex brain environment. Previous research has established abnormal AA fluctuations as a pathological hallmark of epileptic seizures and cytotoxic edema. To further investigate this, we successfully established models of epileptogenesis[45] and excitotoxic neuronal injury[46] through exogenous administration of kainic acid (KA) and *N*-methyl-D-aspartatic acid (NMDA), respectively. As illustrated in Fig. 5A, hematoxylin–eosin (H&E) staining revealed significant neuropathological alterations in C57 mouse models when compared to the control group. These alterations included a disorganized arrangement of pyramidal cells in the hippocampal CA1 region, disrupted annular structures of olfactory bulb glomeruli, and a notable decrease in cell density within the frontal cortex. Collectively, these histopathological features confirm the successful induction of KA-mediated epileptic models.

Research shows that the activation of NMDA glutamate receptors leads to significant increases in Na^+ and Cl^- concentrations within neurons and astrocytes, ultimately causing osmotic cellular swelling and cytotoxic edema.[47] To verify this hypothesis, we first established an Evans blue (EB) standard curve by measuring the absorbance (OD) of EB standard samples at different concentrations (Fig. S30A). Subsequently, we used a spectrophotometer to measure the OD values of brain homogenate supernatants from both the control group (exposed to artificial cerebrospinal fluid, aCSF) and the experimental group (exposed to NMDA) at a wavelength of 620 nm. By referring to the EB standard curve (Fig. S30B), we determined the EB content in both groups, as shown in Fig. 5B and S31. Notably, the EB dye leakage in the NMDA group was approximately three times that of the control group. This is attributed

© 2025 The Author(s). Published by the Royal Society of Chemistry

Open Access Article. Published on 21 October 2025. Downloaded on 6/14/2026 12:59:03 PM.
This article is licensed under a Creative Commons Attribution-NonCommercial 3.0 Unported Licence.

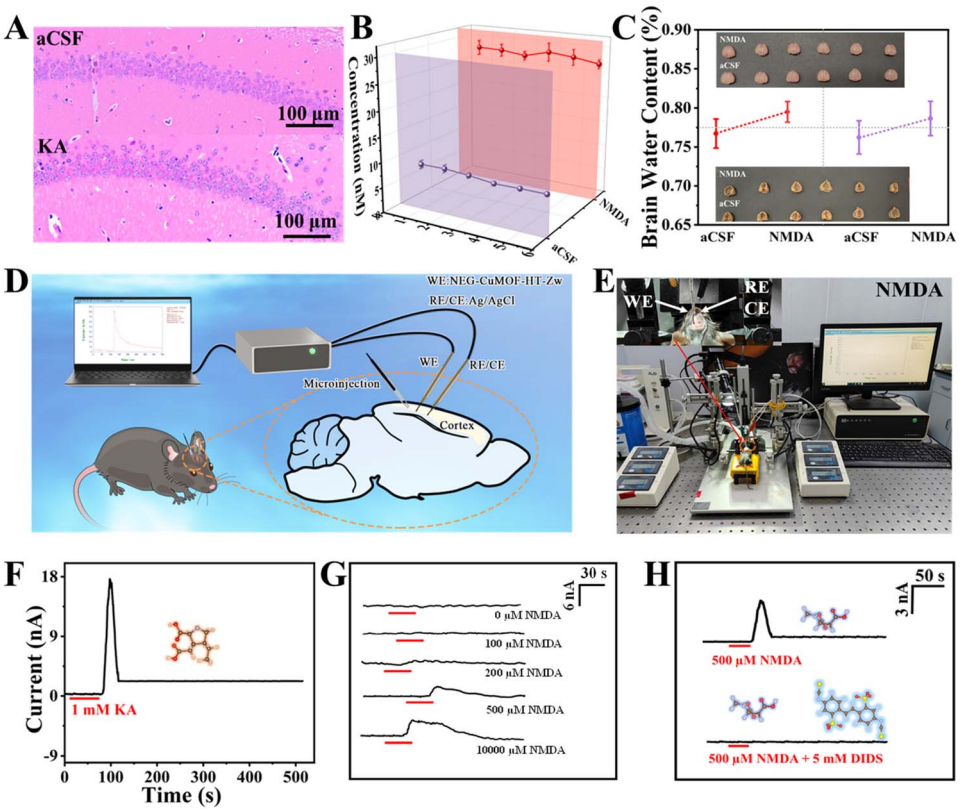

Fig. 5 (A) H&E staining of the hippocampus in the control and epilepsy groups. (B) Changes in Evans blue content in the brains of C57 mice before and after brain edema. (C) BWC in percentage. *X*-axis: BWC (%), *Y*-axis: average value ± SD. aCSF = control group (intact animals); NMDA = NMDA group (edema induced by NMDA). Inset: physical drawings of the aCSF and NMDA groups before and after drying. Error bars indicate the relative standard deviation of three measurements ($n = 3$). (D) Schematic of the AA sensing system for *in vivo* analysis in C57 mouse brains. (E) Diagram of the *in vivo* experimental setup for the cytotoxic edema model. (F) Amperometric currents recorded by NEG-CuMOF-HT-Zw after exogenous injection of 2.5 μL KA into the hippocampus of C57 mice. (G) AA release upon microinjection (1 μL min^{-1} for 60 s, indicated by red lines) of 0–1000 μM NMDA into the cortex of C57 mice. (H) *In vivo* amperometric responses of AA during local microinjection of 500 μM NMDA (1 μL min^{-1} for 60 s) and co-injection of 500 μM NMDA and 5 mM DIDS (1 μL min^{-1} for 300 s). Red lines indicate the microinjection periods. (Each *in vivo* experiment was independently repeated three times with consistent results. Representative curves are shown.)

to the binding of EB to serum proteins (such as albumin),[48] which do not cross the blood–brain barrier under normal physiological conditions, indicating the successful establishment of a mouse model of cerebral edema. To further validate this, we measured the brain water content (BWC) of C57 mice using the dry-wet weighing method (Fig. 5C). The BWC in the experimental group (exposed to NMDA) was significantly higher than that in the control group (exposed to aCSF), also indicating successful induction of cerebral edema by NMDA. Additionally, photographs of mouse brain tissue before and after the dry-wet processing more intuitively demonstrate the morphological changes associated with cerebral edema (inset in Fig. 5C).

For the *in vivo* analysis, C57 mice were securely placed on a scaffold and anesthetized with isoflurane (1.5%). Using a brain locator, the precise detection regions of the hippocampus and cerebral cortex were identified (Fig. 5D, E and S32). Given the potential reduction in sensor sensitivity during *in vivo* testing due to coating by proteins from the surrounding environment, the microsensor's surface was coated with zwitterionic materials to enhance its antifouling capabilities. In this experiment, AA release was monitored in real time in the brains of mice following NMDA-induced cerebral edema. The results demonstrated that the NEG-CuMOF-HT-Zw sensor exhibited a superior current response compared to the other sensors (Fig. S33). Consequently, the NEG-CuMOF-HT-Zw microelectrode was selected for the subsequent investigation of *in vivo* stability. As depicted in Fig. S34, no significant alterations were observed in the current response during the initial hour after the microsensor was inserted into the hippocampal region of the C57 mouse brain. This suggests that this microsensor demonstrated excellent stability for *in vivo* monitoring of AA. Furthermore, as illustrated in Fig. S35, the prompt and reliable current response observed following local administration of AA within the mouse brain demonstrates the sensitivity and specificity of this system in monitoring AA *in vivo*. Taking the epilepsy model as an example, upon local injection of exogenous KA into the hippocampus of C57 mice, there was an elevation in the extracellular AA concentration.[49] Notably, KA itself does not generate a current response (Fig. S36A). Our newly developed microsensor immediately detected a significant response signal within 90 s after the local microinfusion of KA (Fig. 5F), further demonstrating its feasibility for *in vivo* real-time monitoring of dynamic changes in AA levels.

Open Access Article. Published on 21 October 2025. Downloaded on 6/14/2026 12:59:03 PM. This article is licensed under a Creative Commons Attribution-NonCommercial 3.0 Unported Licence.

Furthermore, we confirmed whether the AA release was indeed triggered by cytotoxic edema and delved into the impact of NMDA concentration on AA efflux *in vivo*. Similarly to KA, NMDA does not elicit a current response on its own (Fig. S36B). Specifically, we administered 100, 200, 500, and 1000 μM NMDA into the cortex of C57 mice, employing a NEG-CuMOF-HT-Zw-based microsensor to monitor AA release at a constant infusion rate of 1 μL min^{-1} for 60 s. Fig. 5G illustrates that, in contrast to aCSF injection (0 μM NMDA), minimal amperometric response was observed with 100 μM NMDA infusion, whereas treatments with higher NMDA concentrations elicited substantial current responses. Notably, extracellular AA levels increased by distinct fold (1.5-fold for 200 μM, 2.0-fold for 500 μM, and 2.6-fold for 1000 μM NMDA, respectively, as detailed in Fig. S37), indicating a clear NMDA concentration-dependent AA response. These findings affirm that the AA response of brain tissue to cytotoxic edema follows a defined sequence, underscoring AA's significant potential as a biomarker for indicating cytotoxic edema.

Building upon existing insights into cytotoxic edema mechanisms, we systematically investigated AA release pathways. Critical evidence shows that 4,4′-diisothiocyanatostilbene-2,2′-disulfonic acid (DIDS), a chloride channel blocker, potently suppresses cytotoxic edema by inhibiting cellular swelling-associated Cl^- transport,[47] positioning it as a key pharmacological tool for probing edema-related AA dynamics. Our experimental data demonstrate that 500 μM NMDA administration in C57 mouse brains induces marked extracellular AA accumulation (Fig. 5H).

Strikingly, co-injection of 5 mM DIDS completely abrogates this AA surge while preventing edema development, establishing a direct correlation between cellular swelling inhibition and AA release suppression. This parallel blockade strongly implicates volume-sensitive organic anion channels (VSOACs) as principal mediators of AA efflux (Fig. S38). While prior studies emphasize NMDA-induced AA release through excitotoxicity[50] and glutamate uptake-driven swelling mechanisms,[51] our findings reveal cytotoxic edema itself as an essential regulatory component. The complete abolition of AA release *via* chloride channel blockade indicates that VSOAC activation constitutes a fundamental step rather than a secondary epiphenomenon. Although alternative pathways like glutamate-AA exchange[52] or vesicular exocytosis[53] remain theoretically possible, our controlled co-application paradigm confirms edema-dependent VSOAC activation as a predominant mechanism under these experimental conditions. This edema–AA coupling provides critical mechanistic resolution for understanding neuroinflammatory cascades and excitotoxic injury progression.

Conclusions

In summary, we have developed an innovative CuMOF-HT-based microsensor *via* a chelation-assisted selective etching strategy, which mimics AAO functionality for specific and reliable *in vivo* neurosensing of AA. The His- and Trp-functionalized CuMOF exhibits exceptional AA specificity through hydrogen bonding and π–π stacking interactions. This microsensor demonstrates ultrafast response speed (0.1 s), a low detection limit (1.46 μM), and outstanding stability, enabling precise monitoring of AA dynamics in mouse brains under pathological conditions such as epileptic seizures and cytotoxic edema. Our findings reveal a direct correlation between AA release and cytotoxic edema, supporting the hypothesis that AA efflux depends on edema occurrence. This work highlights the potential of MOF-based nanoenzymes in neurosensing and establishes a platform for real-time, specific, and stable *in vivo* tracking of neurochemicals, advancing brain science and disease research.

Author contributions

Zhao Yang: methodology, conceptualization, software, visualization, validation, writing-original draft, writing – review & editing. Fei Li, Wenbo Huang, and Xikui Ouyang: data characterization and analysis. Tao Huang, Kangbing Wu, and Junxing Hao: supervision, formal analysis, writing – review & editing, funding acquisition, and project administration.

Conflicts of interest

There are no conflicts to declare.

Data availability

The data supporting this article have been included in the main text and the supplementary information (SI). Supplementary information is available. See DOI: **https://doi.org/10.1039/d5sc03207e**.

Acknowledgements

This work was supported by the National Natural Science Foundation of China (No. 22306056 & 22476044) and the Natural Science Foundation of Wuhan (2024040701010050). All animal procedures were performed in accordance with the Guidelines for Care and Use of Laboratory Animals of Hubei University and approved by the Animal Ethics Committee of Hubei University (SYXK 2022-134, Wuhan, China).

Notes and references

1 H. Jin, M. Li, E. Jeong, F. Castro-Martinez and C. S. Zuker, *Nature*, 2024, **630**, 695–703.
2 S. Pidathala, S. Liao, Y. Dai, X. Li, C. Long, C. L. Chang, Z. Zhang and C. H. Lee, *Nature*, 2023, **623**, 1086–1092.
3 S. Sun, J. Li, S. Wang, J. Li, J. Ren, Z. Bao, L. Sun, X. Ma, F. Zheng, S. Ma, L. Sun, M. Wang, Y. Yu, M. Ma, Q. Wang, Z. Chen, H. Ma, X. Wang, Z. Wu, H. Zhang, K. Yan, Y. Yang, Y. Zhang, S. Zhang, J. Lei, Z. Q. Teng, C. M. Liu, G. Bai, Y. J. Wang, J. Li, X. Wang, G. Zhao, T. Jiang, J. C. I. Belmonte, J. Qu, W. Zhang and G. H. Liu, *Nature*, 2023, **624**, 611–620.
4 X. Li, Y. Jin, F. Zhu, R. Liu, Y. Jiang, Y. Jiang and L. Mao, *Angew. Chem., Int. Ed.*, 2022, **61**, e202208121.
5 P. Yu, H. Wei, P. Zhong, Y. Xue, F. Wu, Y. Liu, J. Fei and L. Mao, *Angew. Chem., Int. Ed.*, 2020, **59**, 22652–22658.

© 2025 The Author(s). Published by the Royal Society of Chemistry

Open Access Article. Published on 21 October 2025. Downloaded on 6/14/2026 12:59:03 PM. This article is licensed under a Creative Commons Attribution-NonCommercial 3.0 Unported Licence.

6 J. Liu, Z. Liu, W. Wang and Y. Tian, *Angew. Chem., Int. Ed.*, 2021, **60**, 21351–21359.
7 Y. Wang, Y. Qian, L. Zhang, Z. Zhang, S. Chen, J. Liu, X. He and Y. Tian, *J. Am. Chem. Soc.*, 2023, **145**, 2118–2126.
8 H. Hou, Y. Jin, H. Wei, W. Ji, Y. Xue, J. Hu, M. Zhang, Y. Jiang and L. Mao, *Angew. Chem., Int. Ed.*, 2020, **59**, 18996–19000.
9 M. Bokhove, P. N. Jimenez, W. J. Quax and B. W. Dijkstra, *Proc. Natl. Acad. Sci. U. S. A.*, 2010, **107**, 686–691.
10 G. M. Stoffel, D. A. Saez, H. DeMirci, B. Vögeli, Y. Rao, J. Zarzycki, Y. Yoshikuni, S. Wakatsuki, E. Vöhringer-Martinez and T. J. Erb, *Proc. Natl. Acad. Sci. U. S. A.*, 2019, **116**, 13964–13969.
11 X. Li, W. Tan, J. Fan and K. Li, *ACS Nano*, 2024, **18**, 24162–24172.
12 L. Zuo, K. Ren, X. Guo, P. Pokhrel, B. Pokhrel, M. A. Hossain, Z. X. Chen, H. Mao and H. Shen, *J. Am. Chem. Soc.*, 2023, **145**, 5750–5758.
13 H. B. Aiyappa, P. Wilde, T. Quast, J. Masa, C. Andronescu, Y. T. Chen, M. Muhler, R. A. Fischer and W. Schuhmann, *Angew. Chem., Int. Ed.*, 2019, **58**, 8927–8931.
14 S. Geng, H. Xu, C. S. Cao, T. Pham, B. Zhao and Z. Zhang, *Angew. Chem., Int. Ed.*, 2023, **62**, e202305390.
15 G. Chen, S. Huang, X. Kou, S. Wei, S. Huang, S. Jiang, J. Shen, F. Zhu and G. Ouyang, *Angew. Chem., Int. Ed.*, 2019, **58**, 1463–1467.
16 H. Wang, L. Han, D. Zheng, M. Yang, Y. H. Andaloussi, P. Cheng, Z. Zhang, S. Ma, M. J. Zaworotko, Y. Feng and Y. Chen, *Angew. Chem., Int. Ed.*, 2020, **59**, 6263–6267.
17 S. Dutta, N. Kumari, S. Dubbu, S. W. Jang, A. Kumar, H. Ohtsu, J. Kim, S. H. Cho, M. Kawano and I. S. Lee, *Angew. Chem., Int. Ed.*, 2020, **59**, 3416–3422.
18 H. Sun, Y. Zhou, J. Ren and X. Qu, *Angew. Chem., Int. Ed.*, 2018, **57**, 9224–9237.
19 R. Chapman and M. H. Stenzel, *J. Am. Chem. Soc.*, 2019, **141**, 2754–2769.
20 Z. Yu, Z. Xu, R. Zeng, M. Xu, M. Zou, D. Huang, Z. Weng and D. Tang, *Angew. Chem., Int. Ed.*, 2025, **137**, e202420200.
21 E. Gkaniatsou, C. Sicard, R. Ricoux, L. Benahmed, F. Bourdreux, Q. Zhang, C. Serre, J. P. Mahy and N. Steunou, *Angew. Chem., Int. Ed.*, 2018, **57**, 16141–16146.
22 Y. Kim, T. Yang, G. Yun, M. B. Ghasemian, J. Koo, E. Lee, S. J. Cho and K. Kim, *Angew. Chem., Int. Ed.*, 2015, **54**, 13273–13278.
23 C. C. Hou, L. Zou, Y. Wang and Q. Xu, *Angew. Chem., Int. Ed.*, 2020, **59**, 21360–21366.
24 T. Wang, H. K. Kim, Y. Liu, W. Li, J. T. Griffiths, Y. Wu, S. Laha, K. D. Fong, F. Podjaski, C. Yun, R. V. Kumar, B. V. Lotsch, A. K. Cheetham and S. K. Smoukov, *J. Am. Chem. Soc.*, 2018, **140**, 6130–6136.
25 T. T. Chen, J. T. Yi, Y. Y. Zhao and X. Chu, *J. Am. Chem. Soc.*, 2018, **140**, 9912–9920.
26 Z. Li and H. C. Zeng, *J. Am. Chem. Soc.*, 2014, **136**, 5631–5639.
27 S. Koo, M. G. Lee, A. Sharma, M. Li, X. Zhang, K. Pu, S. G. Chi and J. S. Kim, *Angew. Chem., Int. Ed.*, 2022, **61**, e202110832.
28 M. G. Traber and J. F. Stevens, *Free Radical Biol. Med.*, 2011, **51**, 1000–1013.
29 A. Messerschmidt, R. Ladenstein, R. Huber, M. Bolognesi, L. Avigliano, R. Petruzzelli, A. Rossi and A. Finazzi-Agró, *J. Mol. Biol.*, 1992, **224**, 179–205.
30 L. N. McHugh, M. J. McPherson, L. J. McCormick, S. A. Morris, P. S. Wheatley, S. J. Teat, D. McKay, D. M. Dawson, C. E. Sansome and S. E. Ashbrook, *Nat. Chem.*, 2018, **10**, 1096–1102.
31 P. Falcaro, K. Okada, T. Hara, K. Ikigaki, Y. Tokudome, A. W. Thornton, A. J. Hill, T. Williams, C. Doonan and M. Takahashi, *Nat. Mater.*, 2017, **16**, 342–348.
32 Z. Wang, Y. Huang, K. Xu, Y. Zhong, C. He, L. Jiang, J. Sun, Z. Rao, J. Zhu and J. Huang, *Nat. Commun.*, 2023, **14**, 69.
33 X. Zhou, H. Jin, B. Y. Xia, K. Davey, Y. Zheng and S. Z. Qiao, *Adv. Mater.*, 2021, **33**, 2104341.
34 D. Chen, Z. Xia, Z. Guo, W. Gou, J. Zhao, X. Zhou, X. Tan, W. Li, S. Zhao and Z. Tian, *Nat. Commun.*, 2023, **14**, 7127.
35 C. Tao, Y. Jiang, S. Chu, Y. Miao, J. Zhang, Y. Lu and L. Niu, *Anal. Chem.*, 2024, **96**, 3107–3115.
36 L. Liu, L. Lei, K. Zeng, K. Wu and N. Yang, *Adv. Funct. Mater.*, 2023, **33**, 2211335.
37 J. Zhang, C. Li, H. Wang, Z. Yang, C. Hu, K. Wu, J. Hao and Z. Liu, *Anal. Chem.*, 2023, **95**, 18907–18916.
38 J. Hao, Z. Zhu, C. Hu and Z. Liu, *Anal. Chem.*, 2022, **94**, 4547–4555.
39 D. Meng, C. Hao, J. Cai, W. Ma, C. Chen, C. Xu, L. Xu and H. Kuang, *Angew. Chem., Int. Ed.*, 2021, **133**, 25201–25208.
40 S. Wei, W. Ma, M. Sun, P. Xiang, Z. Tian, L. Mao, L. Gao and Y. Li, *Nat. Commun.*, 2024, **15**, 6888.
41 B. Cao, C. J. Lee, Z. Zeng, F. Cheng, F. Xu, H. Cong and G. Cheng, *Chem. Sci.*, 2016, **7**, 1976–1981.
42 H. Wang, C. Li, J. Zhang, Z. Yang, J. Li, Y. Cao, K. Wu, Z. Liu, J. Hao and X. Ye, *Adv. Funct. Mater.*, 2024, **34**, 2315917.
43 M. Agathocleous, C. E. Meacham, R. J. Burgess, E. Piskounova, Z. Zhao, G. M. Crane, B. L. Cowin, E. Bruner, M. M. Murphy and W. Chen, *Nature*, 2017, **549**, 476–481.
44 D. Liu, M. Rahman, A. Johnson, R. Amo, I. Tsutsui-Kimura, Z. A. Sullivan, N. Pena, M. Talay, B. L. Logeman and S. Finkbeiner, *Nature*, 2025, **640**, 1000–1010.
45 T. Xiao, Y. Jiang, W. Ji and L. Mao, *Anal. Chem.*, 2018, **90**, 4840–4846.
46 J. Jin, W. Ji, L. Li, G. Zhao, W. Wu, H. Wei, F. Ma, Y. Jiang and L. Mao, *J. Am. Chem. Soc.*, 2020, **142**, 19012–19016.
47 R. L. Rungta, H. B. Choi, J. R. Tyson, A. Malik, L. Dissing-Olesen, P. J. Lin, S. M. Cain, P. R. Cullis, T. P. Snutch and B. A. MacVicar, *Cell*, 2015, **161**, 610–621.
48 W. Cheng, W. Zhang, X. Xia, J. Zhang, M. Wang, Y. Li, X. Li, Y. Zheng, J. Liu and R. Zhang, *Nano Today*, 2023, **48**, 101721.
49 W. Ji, K. Liu, G. Zhao, F. Wu, Y. Jiang, L. Hou, M. Zhang and L. Mao, *ACS Sens.*, 2021, **6**, 546–552.
50 J. M. May, *Subcell. Biochem.*, 2012, **56**, 85–103.
51 D. J. Lane and A. Lawen, *Cell Biochem. Biophys.*, 2013, **65**, 107–119.
52 J. Cammack, B. Ghasemzadeh and R. Adams, *Brain Res.*, 1991, **565**, 17–22.
53 K. Wang, T. Xiao, Q. Yue, F. Wu, P. Yu and L. Mao, *Anal. Chem.*, 2017, **89**, 9502–9507.